Medical Image Analysis 99 (2025) 103369

Contents lists available at ScienceDirect

Medical Image Analysis

journal homepage: www.elsevier.com/locate/media

SpinDoctor-IVIM: A virtual imaging framework for intravoxel incoherent motion MRI

Mojtaba Lashgari [a], Zheyi Yang [b], Miguel O. Bernabeu [c], Jing-Rebecca Li [b], Alejandro F. Frangi [a,d,e,f,g,h,*]

[a] Centre for Computational Imaging and Simulation Technologies in Biomedicine (CISTIB), School of Computing, University of Leeds, Leeds, UK
[b] Inria-Saclay, Equipe Idefix, ENSTA Paris, Unite de Mathematiques Appliquees (UMA), 91762 Palaiseau, France
[c] Centre for Medical Informatics, Usher Institute, The University of Edinburgh, Edinburgh, UK
[d] Christabel Pankhurst Institute, Division of Informatics, Imaging and Data Sciences, School of Health Sciences, University of Manchester, UK
[e] Christabel Pankhurst Institute, Department of Computer Science, School of Engineering, University of Manchester, UK
[f] Medical Imaging Research Centre (MIRC), Department of Cardiovascular Sciences, KU Leuven, Leuven, Belgium
[g] Medical Imaging Research Centre (MIRC), Department of Electrical Engineering, KU Leuven, Leuven, Belgium
[h] Alan Turing Institute, London, UK

ARTICLE INFO

MSC:
41A05
41A10
65D05
65D17

Keywords:
Generalised Bloch–Torrey equation
Diffusion magnetic resonance imaging
Finite element method
Virtual imaging
Intravoxel incoherent motion imaging

ABSTRACT

Intravoxel incoherent motion (IVIM) imaging is increasingly recognised as an important tool in clinical MRI, where tissue perfusion and diffusion information can aid disease diagnosis, monitoring of patient recovery, and treatment outcome assessment. Currently, the discovery of biomarkers based on IVIM imaging, similar to other medical imaging modalities, is dependent on long preclinical and clinical validation pathways to link observable markers derived from images with the underlying pathophysiological mechanisms. To speed up this process, virtual IVIM imaging is proposed. This approach provides an efficient virtual imaging tool to design, evaluate, and optimise novel approaches for IVIM imaging. In this work, virtual IVIM imaging is developed through a new finite element solver, SpinDoctor-IVIM, which extends SpinDoctor, a diffusion MRI simulation toolbox. SpinDoctor-IVIM simulates IVIM imaging signals by solving the generalised Bloch–Torrey partial differential equation. The input velocity to SpinDoctor-IVIM is computed using HemeLB, an established Lattice Boltzmann blood flow simulator. Contrary to previous approaches, SpinDoctor-IVIM accounts for volumetric microvasculature during blood flow simulations, incorporates diffusion phenomena in the intravascular space, and accounts for the permeability between the intravascular and extravascular spaces. The above-mentioned features of the proposed framework are illustrated with simulations on a realistic microvasculature model.

1. Introduction

Intravoxel incoherent motion (IVIM) imaging is a diffusion magnetic resonance imaging (dMRI) technique that allows the evaluation of blood perfusion in tissue. IVIM refers to the transitional displacement of water molecules' spins within an MRI voxel during the measurement time. This leads to a distribution of spin speeds, affecting both the orientation and/or the amplitude of the spins's speed (Le Bihan et al., 1986). This distribution originates from the blood flowing within a microvascular network, e.g., Fig. 1.a, and mimics a pseudo-diffusion process. The pseudo-diffusion process results in a faster decay of the dMRI signal in the presence of diffusion encoding gradients, as depicted in Fig. 1.b (Jerome et al., 2021). Being an endogenous contrast technique and providing local information about both perfusion (excitation and readout are carried out in the same plane) and tissue microstructure (through the diffusion of water molecules in the extravascular space) are the main advantages of IVIM imaging that make it suitable for clinical use (Federau, 2017).

1.1. Problem statement

Recent literature on IVIM imaging has revealed the feasibility of *in vivo* implementation of IVIM imaging using the current clinical setting (Iima and Le Bihan, 2016; Federau et al., 2014). IVIM imaging is sufficiently sensitive to capture physiological and drug-induced changes in tissue perfusion (Federau, 2017). However, IVIM imaging suffers from a low contrast-to-noise ratio due to the small perfusion fraction (tissue blood volume fraction) in many organs. For example,

* Centre for Computational Imaging and Simulation Technologies in Biomedicine (CISTIB), School of Computing, University of Leeds, Leeds, UK.
E-mail addresses: m.lashgari@leeds.ac.uk (M. Lashgari), alejandro.frangi@manchester.ac.uk (A.F. Frangi).

https://doi.org/10.1016/j.media.2024.103369
Received 21 October 2023; Received in revised form 3 October 2024; Accepted 5 October 2024
Available online 16 October 2024

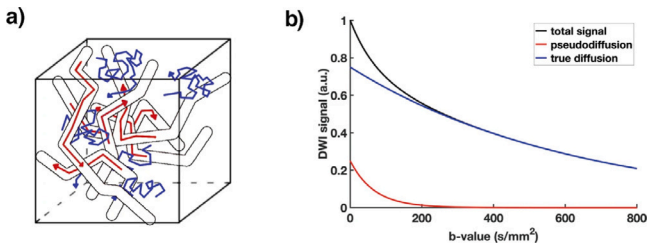

Fig. 1. IVIM model. (a) A schematic illustrating water molecules' transitional movement in the intravascular space (depicted in red) and Brownian motion in the extravascular space (depicted in blue) within a tissue voxel. (b) A comparison of the observed dMRI signal decays based on the Brownian movement of water molecules (diffusion) and transitional movement of water molecules (pseudo diffusion). Pseudo-diffusion contributes significantly faster signal decays than diffusion and is thus observed only at low b-values. Image reproduced with permission (Jerome et al., 2021).

the perfusion fraction comprises 5% of the whole brain volume (Zhang et al., 2018) and 13% of the whole heart volume (Spinner et al., 2019). Consequently, uncertainties remain regarding the exact relationship between the parameters of IVIM imaging, i.e., pseudo-diffusion, perfusion fraction, and tissue diffusion. Therefore, there is abundant interest in research to advance our understanding of the sensitivity of IVIM imaging parameters to the biophysical features of the microvasculature and imaging protocol. In addition, there is interest in investigating the feasibility of estimating microvascular biophysical parameters from IVIM imaging data. Finally, it is of particular interest to discover the exact role of other sources of IVIM, such as arterioles/veins and other fluid flows such as cerebrospinal fluid of the brain in addition to the capillaries, which are not fully understood.

These questions can be investigated by virtual imaging, as it provides full control over the structure of microvasculature and extravascular compartments, along with imaging protocols (Fieremans and Lee, 2018). Although extensive research has been conducted on the clinical application of IVIM imaging (Iima and Le Bihan, 2016), only a few studies have shed light on the potential of virtual imaging to improve the interpretation of IVIM imaging signals.

1.2. Previous method

To date, all numerical studies of IVIM imaging have been performed using a simple numerical method, namely an elementary method. This method simulates spin displacements based only on constant blood flow velocities along vascular trajectories $R(t')$, not in vascular lumens. Then, the acquired phase ϕ_t due to these spin displacements is computed as

$$\phi_t = \int_0^t \gamma G(t')(R(t'), t')dt' \tag{1}$$

and finally, the approximate IVIM imaging signal is computed using

$$S = S_0 \mathbb{E}\{e^{(i\phi_t)}\} \tag{2}$$

where $\mathbb{E}\{\}$ is an expectation of random variable of ϕ_t (Fournet et al., 2017). Mozumder et al. (2018) used this method to analyse the sensitivity of different IVIM imaging parameter estimation algorithms to the parameter initialisation values. Furthermore, Spinner et al. (2019) used the same method to compare the efficacy of IVIM imaging encoding of spin-echo and stimulated-echo-based diffusion MRI to assess myocardial perfusion. In another work, using this method, IVIM imaging was simulated in three realistic vascular networks of a mouse brain (Van et al., 2021).

A likely explanation for the limited body of research on the virtual study of IVIM imaging, compared to dMRI (Fieremans and Lee, 2018), is the lack of a sophisticated virtual imaging technique for IVIM imaging simulation. The major drawback of the above elementary approach is the use of the vessel trajectory instead of the 3D geometry of the microvasculature, which imposes the following limitations.

1. The water molecules' diffusion within the intravascular space due to the Brownian motion is ignored.
2. The effect of the permeability between the intravascular and extravascular spaces on the IVIM imaging signal cannot be explained.
3. The simulation of blood flow is unrealistic, as the elementary method assigns a unique blood velocity to each segment of the vessel. However, the velocity of blood along both parallel and vertical axes of the vessel axis is variable.

1.3. Motivation and contribution

The objective of this paper is to present a virtual IVIM imaging framework that overcomes the limitations mentioned above. To achieve this, we expand an MR transverse magnetisation solver/simulator initially developed by Li et al. (2019). This extension enables us to solve the generalised Bloch–Torrey partial differential equation (gBT PDE), which considers the velocity of the spins, in contrast to the conventional BT PDE. (The significance of the difference between conventional BT and gBT equations has been explained in Section 2). This extended simulation tool is referred to as "SpinDoctor-IVIM", as it allows the simulation of IVIM imaging.

The local blood flow velocities within microvasculature, required inputs for SpinDoctor-IVIM, are derived by employing a pre-existing HemeLB blood flow simulator. It is important to note that both SpinDoctor-IVIM and HemeLB consider the entire 3D volume of the microvasculature, as opposed to solely focusing on skeleton or trajectory of microvasculature. Fig. 2 shows the schematic diagram of this virtual IVIM imaging framework.

The next section concerns the theory used to develop the proposed virtual IVIM imaging framework. First, the key principles of the blood flow model, used to compute the local velocity of blood flow within a microvasculature, along with the gBT equation, which underpins the SpinDoctor-IVIM, are explained. Section 3 describes the data used in this paper. Section 4 is concerned with the methodological development of this study. Section 5 validates the proposed solution for gBT PDE. Section 6 presents the proposed tool, focussing on the key opportunities provided by the new tool to study tissue perfusion using virtual IVIM imaging. Finally, Section 7 discusses the results, limitations, and future work.

2. Theory

This section describes the Navier–Stokes and generalised Bloch–Torrey equations as the theoretical foundations for simulating blood flow and MR transverse magnetisation using HemeLB and SpinDoctor-IVIM, respectively.

2.1. Navier–Stokes equation

Given the viscoelastic properties of blood and the length scales assumed, blood is considered an incompressible non-Newtonian fluid (Baieth, 2008). The flow of an incompressible and non-Newtonian fluid in an observation domain of Ω is governed by the Navier–Stokes equations, Eq. (3), where $\boldsymbol{v}(\boldsymbol{r}, t)$ is the flow velocity, ϑ is a dynamic viscosity parameter, and $P(\boldsymbol{r}, t)$ is the pressure.

$$\rho\Big(\frac{\partial}{\partial t}\boldsymbol{v}(\boldsymbol{r}, t) + \big(\boldsymbol{v}(\boldsymbol{r}, t)\cdot\nabla\big)\boldsymbol{v}(\boldsymbol{r}, t)\Big) = \vartheta\Delta\boldsymbol{v}(\boldsymbol{r}, t) + \nabla P(\boldsymbol{r}, t) \quad (\boldsymbol{r}\in\Omega), \tag{3}$$

$$\nabla\cdot\boldsymbol{v}(\boldsymbol{r}, t) = 0 \qquad (\boldsymbol{r}\in\Omega), \tag{4}$$

subject to the boundary conditions

$$\boldsymbol{v}(\boldsymbol{r}, t) = 0 \qquad (\boldsymbol{r}\in\Gamma_w), \tag{5}$$

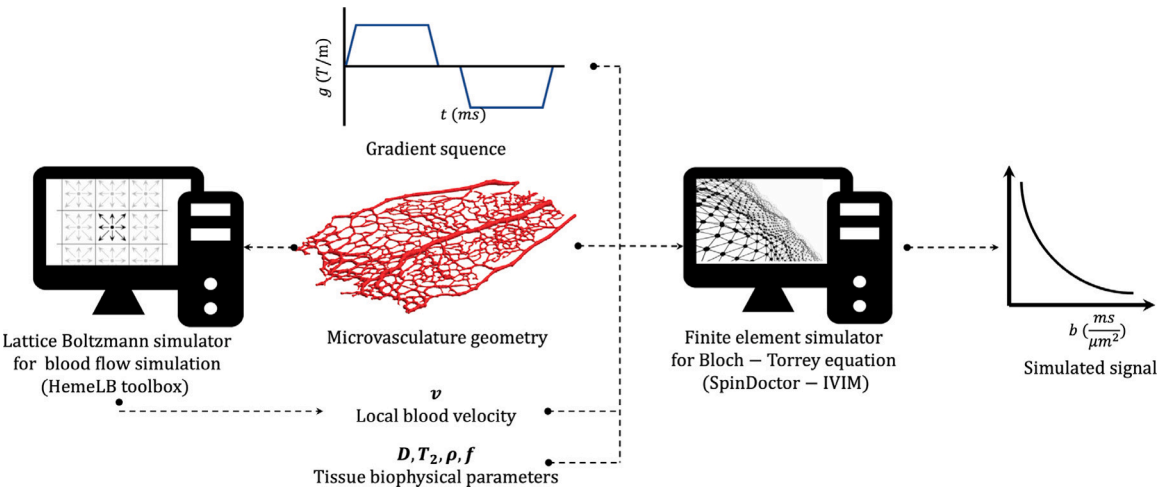

Fig. 2. Schematic diagram of the proposed integrated tool for virtual IVIM imaging.

$$P(\boldsymbol{r},t)\cdot\boldsymbol{n}(\boldsymbol{r})-\frac{\vartheta}{\rho}\nabla\boldsymbol{v}(\boldsymbol{r},t)\cdot\boldsymbol{n}(\boldsymbol{r})=P(\boldsymbol{r},t)\cdot\boldsymbol{n}(\boldsymbol{r}) \quad (\boldsymbol{r}\in\Gamma_i\cup\Gamma_o), \tag{6}$$

and the initial condition

$$\boldsymbol{v}(\boldsymbol{r},0)=0, \tag{7}$$

where $\boldsymbol{r}\in\Gamma_w$, $\boldsymbol{r}\in\Gamma_i$, and $\boldsymbol{r}\in\Gamma_o$, respectively, are the wall, inlet and outlet portions of the vascular boundary domains.

In non-Newtonian fluids, ϑ has a functional form that is given based on the Carreau–Yasuda mathematical model:

$$\vartheta(\dot{Y})=\vartheta_\infty+(\vartheta_0-\vartheta_\infty)\times[1+(\lambda\dot{Y})^a]^{(\frac{n-1}{a})}, \tag{8}$$

where $\vartheta_0 = 14.49\,\text{mPa s}$, $\vartheta_\infty = 3.265\,\text{mPa s}$, $\lambda = 0.1839\,\text{s}$, $a = 2.707$, $n = 0.4136$ are computed as explained in Bernabeu et al. (2014). $\dot{Y}$ is the shear rate:

$$\dot{Y}=\sqrt{2S_{ij}S_{ij}} \tag{9}$$

which depends on the stress tensor:

$$S_{ij}=\frac{1}{2}\left(\frac{\partial v_i}{\partial x_i}+\frac{\partial v_j}{\partial x_j}\right) \tag{10}$$

where $i,j=1,2,3$ and summation over repeated indices is assumed.

HemeLB is a computational fluid dynamics package that resolves the full three-dimensional flow field in any microvascular bed of interest by approximating the Navier–Stokes equations with an efficient and highly parallel LBM (Lattice Boltzmann Method) implementation (Mazzeo and Coveney, 2008).

As explained in the introduction, the pseudo-diffusion coefficient characterises the blood flow through the capillaries as a diffusion-like process and relates it to the velocity of blood flow. Therefore, having a more realistic and accurate IVIM imaging simulation requires a more realistic and accurate blood flow simulation that is achievable through HemeLB. A more detailed description of HemeLB is available in Mazzeo and Coveney (2008).

2.2. Generalised Bloch–Torrey equation

The transverse magnetisation signal can be mathematically described with the Bloch–Torrey equation, Eq. (11), which relates the temporal and spatial evolution of transverse magnetisation $M(\boldsymbol{r},t)$ to diffusion $D(\boldsymbol{r})$, spin–spin relaxation T_2, and the time-varying magnetic field gradient $f(t)\boldsymbol{g}\cdot\boldsymbol{r}$, where $f(t)$ is the effective time profile and $\boldsymbol{g}$ contains the amplitude and directional information of the magnetic field gradient. Let Ω be the observation domain comprising subdomains of L, such that $\Omega=\cup_{l=1}^{L}\Omega_l$. Also, let Γ_{ln} represent the boundary between Ω_l and Ω_n. Then, the evolution of the complex transverse magnetisation is described by:

$$\frac{\partial}{\partial t}M_l(\boldsymbol{r},t)=\nabla\cdot(D_l(\boldsymbol{r})\nabla M_l(\boldsymbol{r},t))-\frac{1}{T_{2l}}M_l(\boldsymbol{r},t)-i\gamma f(t)\boldsymbol{g}\cdot\boldsymbol{r}M_l(\boldsymbol{r},t) \quad (\boldsymbol{r}\in\Omega_l), \tag{11}$$

subject to the boundary conditions:

$$D_l(\boldsymbol{r})\nabla M_l(\boldsymbol{r},t).\boldsymbol{n}_l(\boldsymbol{r})=P_{ln}(M_n(\boldsymbol{r},t)-M_l(\boldsymbol{r},t)) \quad (\boldsymbol{r}\in\Gamma_{nl},\forall n), \tag{12}$$

and magnetisation flux conservation between adjacent layers:

$$D_l(\boldsymbol{r})\nabla M_l(\boldsymbol{r},t).\boldsymbol{n}_l(\boldsymbol{r})=-D_n(\boldsymbol{r})\nabla M_n(\boldsymbol{r},t).\boldsymbol{n}_n(\boldsymbol{r}) \quad (\boldsymbol{r}\in\Gamma_{ln}), \tag{13}$$

and the initial condition:

$$M_l(\boldsymbol{r},0)=\rho_l(\boldsymbol{r}), \tag{14}$$

where $t\in[0,T_E]$ with T_E echo time, $\boldsymbol{n}_l(\boldsymbol{r})$ is the unitary outward pointing normal to Ω_l, P_{ln} is the permeability constant in Γ_{ln}. Furthermore, the same permeability is assumed in both directions of the membrane, that is, $P_{ln}=P_{nl}$.

SpinDoctor is a Matlab toolbox to simulate transverse magnetisation by providing numerical solutions to the BT PDE (Li et al., 2019). The new extension of SpinDoctor, SpinDoctor-IVIM, however, takes into account the velocity of the water molecules' spins in the blood flow alongside their diffusion and relaxation by solving gBT PDE, defined by adding velocity of flow $\boldsymbol{v}(\boldsymbol{r},t)$ in the medium in the Eq. (11):

$$\frac{\partial}{\partial t}M_l(\boldsymbol{r},t)=\nabla\cdot(D_l(\boldsymbol{r})\nabla M_l(\boldsymbol{r},t))-\frac{1}{T_{2l}}M_l(\boldsymbol{r},t)-i\gamma f(t)\boldsymbol{g}\cdot\boldsymbol{r}M_l(\boldsymbol{r},t)-\boldsymbol{v}(\boldsymbol{r},t)\cdot\nabla M_l(\boldsymbol{r},t) \quad (\boldsymbol{r}\in\Omega_l), \tag{15}$$

3. Data

This study uses a transmission electron image of a retinal vascular plexus network, shown in the centre of Fig. 2, due to a limited number of inlets and outlets in the network (Bernabeu et al., 2014). The use of complex microvasculature, encompassing numerous inlets and outlets, requires a preprocessing approach to differentiate between inlets and outlets. Additionally, it involves the assignment of physiologically accurate boundary conditions. However, addressing these aspects is beyond the scope of this paper and is reserved for future research studies.

Details regarding tissue preparation and transmission electron microscopy imaging, along with image segmentation and 3D surface

generation, are available in Franco et al. (2008) and Bernabeu et al. (2014), respectively. In this network, the largest diameter is 40 μm, which occurs along the retinal vein, while the larger diameter of the artery segments is approximately 16 μm approaching the optic disc. The diameters of the capillaries vary approximately in the range 2 to 10 μm, with a reduced number of vessels with a smaller diameter.

4. Method

4.1. Finite element solution of generalised bloch–torrey partial differential equation

This section presents a mathematical contribution to extend the original version of SpinDoctor to the SpinDoctor-IVIM version. The gBT equation, Eq. (15), is spatially discretised using the finite element method (FEM), similar to the BT in Li et al. (2019), resulting in the following linear system:

$$\boldsymbol{M}_l \frac{\delta \eta_l}{\delta t} = -(\boldsymbol{S}_l + \sqrt{-1}\boldsymbol{Q}_l(t) + \frac{1}{T_l}\boldsymbol{M}_l + \boldsymbol{J}_l + \boldsymbol{F}_l(t))\eta_l, \tag{16}$$

where

$$\{\boldsymbol{M}_l\}_{ij} \overset{\Delta}{=} M_{ij} = \int_{\Omega_l} \phi_j^l(\boldsymbol{r})\phi_i^l(\boldsymbol{r})\, d\boldsymbol{r} \tag{17}$$

is the mass matrix,

$$\{\boldsymbol{S}_l\}_{ij} \overset{\Delta}{=} S_{ij} = \int_{\Omega_l} \nabla\phi_j^l(\boldsymbol{r})\boldsymbol{D}_l\nabla\phi_i^l(\boldsymbol{r})\, d\boldsymbol{r} \tag{18}$$

is the stiffness matrix,

$$\{\boldsymbol{Q}_l\}_{ij}(t) \overset{\Delta}{=} Q_{ij}(t) = \gamma \int_{\Omega_l} \phi_j^l(\boldsymbol{r})\phi_i^l(\boldsymbol{r}) f(t)\boldsymbol{g}\cdot\boldsymbol{r}\, d\boldsymbol{r} \tag{19}$$

is the scaled-mass matrix,

$$\{\boldsymbol{J}_l\}_{ij} \overset{\Delta}{=} J_{ij} = \begin{cases} \kappa_{ln}\int_{\Gamma_{ln}} \phi_j^l(\boldsymbol{r})\phi_i^l(\boldsymbol{r})d\boldsymbol{r}, \\ -\kappa_{ln}\int_{\Gamma_{ln}} \phi_j^n(\boldsymbol{r})\phi_i^l(\boldsymbol{r})d\boldsymbol{r}. \end{cases} \tag{20}$$

is the flux matrix, and

$$\{\boldsymbol{F}_l\}_{ij} \overset{\Delta}{=} F_{ij} = \int_{\Omega_l} \phi_j^l(\boldsymbol{r})\boldsymbol{v}(\boldsymbol{r},t)\cdot\nabla\phi_i^l(\boldsymbol{r})\, d\boldsymbol{r} \tag{21}$$

is the damping matrix. The finite elements used by SpinDoctor-IVIM are P1 elements, η_l is the approximation of the magnetisation at the nodes of the finite element in Ω_l, and $(\phi_i^l(\boldsymbol{r}))$ are the set of finite element basis functions in Ω_l.

SpinDoctor utilises equations Eq. (17)–(20) to solve the BT equation. However, SpinDoctor-IVIM further integrates the damping matrix as described in Eq. (21) into the linear system presented in Eq. (16). The linear system of Eq. (16) is solved using the *theta time-stepping method* (generalised midpoint method) (Stuart and Peplow, 1991), with the following parameter setup:

- *implicitness* = 0.5: calls Crank Nicolson method (Stuart and Peplow, 1991);
- *timestep* = 5 μs: timestep for iterations.

4.2. Interpolating local velocities for tetrahedron mesh

As described above, HemeLB calculates the local velocities of the intravascular spins, which are required as input to SpinDoctor-IVIM. HemeLB employs lattice-based spatial discretisation, where the values of the local velocities are computed at the vertices of the lattice, represented as small circles in Fig. 3. However, it is imperative to compute these local velocities for each tetrahedron, since tetrahedral meshes serve as input for SpinDoctor-IVIM. Fig. 3 illustrates the generation of tetrahedrons in various sizes, which occupy computational space without sharing vertices with the lattice. Consequently, interpolation of local velocities for the centres of each tetrahedron is necessary before simulating the IVIM imaging signal with SpinDoctor-IVIM.

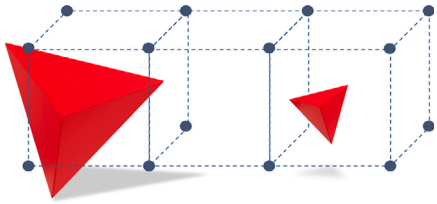

Fig. 3. A schematic of the relative position of a lattice versus tetrahedron.

Prior to interpolation, aligning the discretised domains of the lattice and the tetrahedral mesh is essential for achieving highly accurate velocity interpolation at the centres of tetrahedrons. The most efficient approach to attaining this alignment is to directly create a tetrahedral volume mesh from the input surface mesh used in HemeLB, as shown in Fig. 4a. However, there are instances where the tetrahedral volume mesh may not achieve full alignment with the lattice domain. Consequently, before velocity interpolation, a thorough investigation and correction of the mesh registration between the two domains is necessary, as illustrated in Fig. 4.

To achieve this, initially, a rigid transformation is calculated to align the tetrahedral domain surface with the HemeLB input mesh surface (Chen and Medioni, 1992; Besl and McKay, 1992). Subsequently, utilising this rigid transformation, all vertices within the tetrahedral domain are relocated to new positions. Once the tetrahedral domain is successfully registered with the lattice domain, the velocity values at the centres of the tetrahedrons are interpolated using scattered data interpolation techniques (Amidror, 2002).

4.3. Adding extravascular domain

The impact of microvasculature permeability on the IVIM imaging signal can be accounted for by enclosing the microvasculature within extravascular spaces, as illustrated in Fig. 5. The outline boundary of this extravascular space can, however, affect the simulated signal unrealistically. Unlike real tissue, which does not have these boundaries, molecules that reach this extravascular space in the simulation domains reflect elastically off. To eliminate the impact of collisions between molecules and extravascular outline boundaries in the simulation domain, IVIM imaging simulations are conducted over a mesh with a larger extravascular domain. The extravascular magnetisations in the vicinity of the outline boundaries are then excluded from the IVIM imaging signal calculation.

4.4. Removing effect of outlet boundaries on a simulated IVIM imaging

In virtual IVIM imaging, when simulated spins reach the outlet boundaries, they undergo elastic reflection, which affects the simulated signal. Such collisions, which influence the signal, do not occur in real IVIM imaging experiments due to the continuous nature of the vascular system. Hence, it is essential to configure the simulation parameters in a way that prevents spins from reaching the outlet boundaries prior to the echo time. For this purpose, virtual IVIM imaging begins in a part of the vascular domain, referred to as "region of interest" (ROI), shown in Fig. 6. This ROI is positioned at a considerable distance from the outlet boundaries. At the same time, the noninterest region (RONI), situated close to the outlet boundaries, is initialised with zero magnetisation, as shown in Fig. 6. Finally, once the simulation is concluded, the simulated IVIM imaging signal is derived without taking into account the magnetisation values within the RONI.

As depicted in Fig. 6, a reliable and straightforward method to delineate RONI within the domain is to encompass the area around the outlet boundaries up to a distance of $\max\{\boldsymbol{v}(\boldsymbol{r},t)\} \times T_e$ where T_e represents the echo time. Fig. 7 displays examples of the simulated IVIM

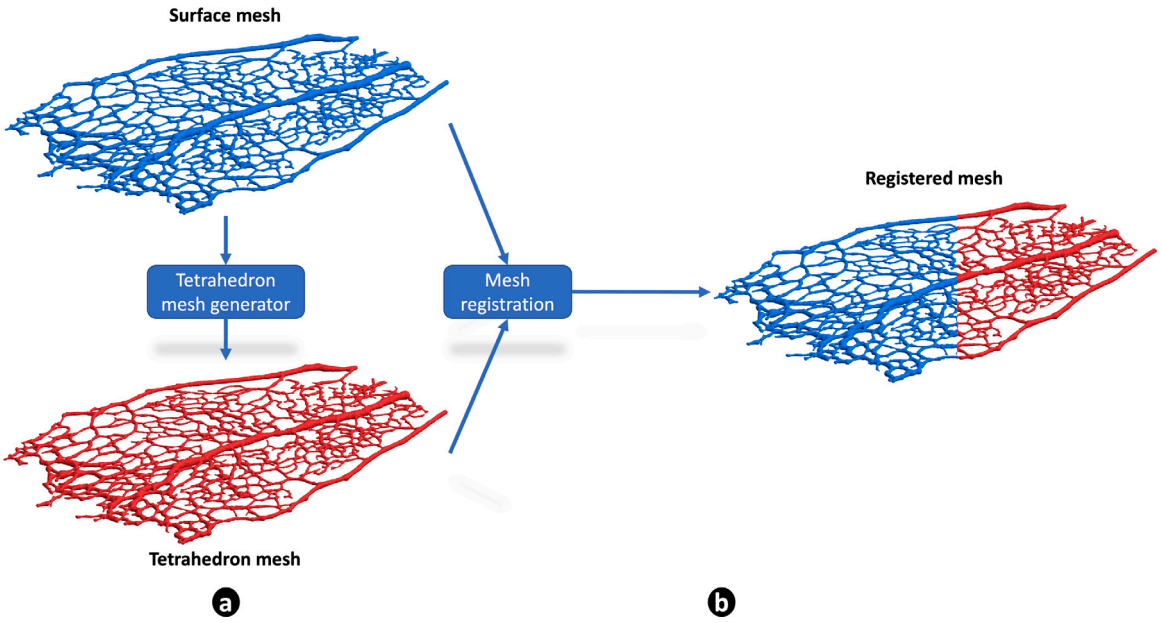

Fig. 4. Mesh generation and registration. (a) Generating the tetrahedron mesh, to be used as the SpinDoctor IVIM input, from the input surface mesh of HemeLB; (b) Registration between the tetrahedron mesh and the output lattice of HemeLB.

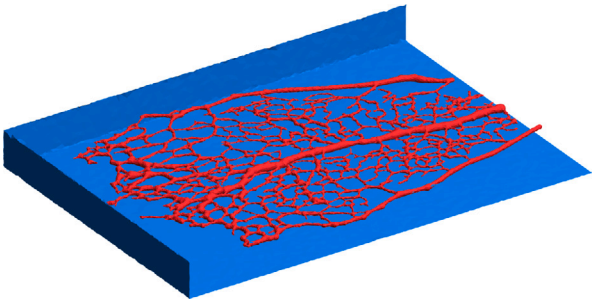

Fig. 5. Sub-set of murine retinal vascular plexus (red) surrounded by extra-vascular space (blue).

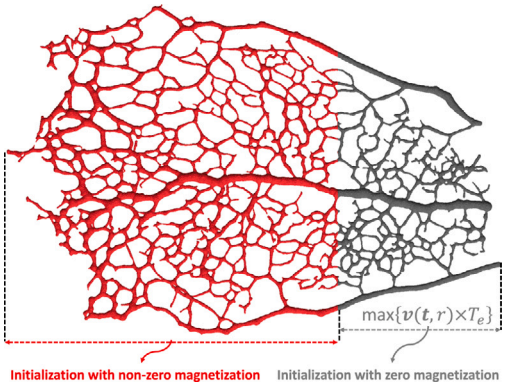

Fig. 6. Excluding the effect of the outlet boundaries on the simulated IVIM imaging signal by setting zero initial magnetisation at $\max\{\boldsymbol{v}(\boldsymbol{r},t)\} \times T_e$ vicinity of outlet boundaries. At the end of the simulation, the magnetisation in this region is dismissed in the computation of the final signal.

imaging signal for various ROI with velocities ranging from 0 to the maximum achievable velocity within each ROI.

In all the experiments carried out in this study, the calculation of local blood flow velocities within the microvasculature is based on the findings of a blood flow simulation reported in Bernabeu et al. (2014), conducted under an ocular perfusion pressure of 25 mmHg. In the same study, variations in ocular perfusion pressure were established to only affect the magnitude of blood velocity within the microvasculature, while the flow pattern remains unchanged. Consequently, to replicate the IVIM imaging simulation at different blood pressures, the magnitude of simulated velocities for an ocular perfusion pressure of 25 mmHg is proportionally adjusted.

5. Validation

To ensure the precision and reliability of SpinDoctor-IVIM, we conducted a comparative analysis of the average magnetisation and signal intensity simulated within a cylindrical structure measuring 5 μm in radius and 100 μm in length. These results were juxtaposed with those obtained from a well-established software, COMSOL (Tennyson, 2014; Oliveira, 2021), on a range of various b-values and spin velocities. In this experiment, we iterated the simulation using three distinct velocities, where the magnitude of the velocities remained constant at $0.005, 0.01, 0.02\,\mathrm{m\,s^{-1}}$, while their directions were parallel to the

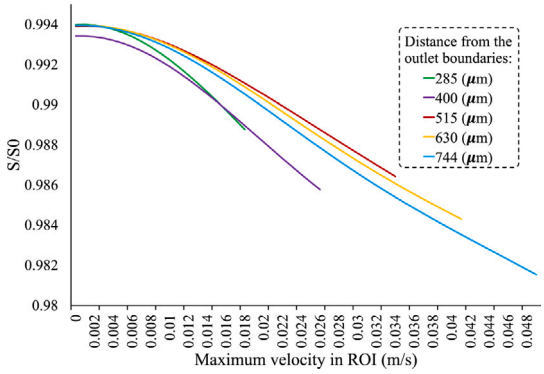

Fig. 7. Effect of different ROIs, i.e., $\max\{\boldsymbol{v}(\boldsymbol{r},t)\} \times T_e$, and maximum velocities $\max\{\boldsymbol{v}(\boldsymbol{r},t)\}$ for each ROI on normalised IVIM imaging signal.

cylinder's axis for all spins. The b-values include $10, 20, 40, 80, \ldots, 2560, 5120, 10240\,\mathrm{s\,mm^{-2}}$, with $\delta = 10\,\mathrm{ms}$ and $\Delta = 40\,\mathrm{ms}$. As depicted in Figs. 8 and 9, the averaged magnetisation and signal intensity obtained from SpinDoctor-IVIM agree closely with those calculated by COMSOL. The

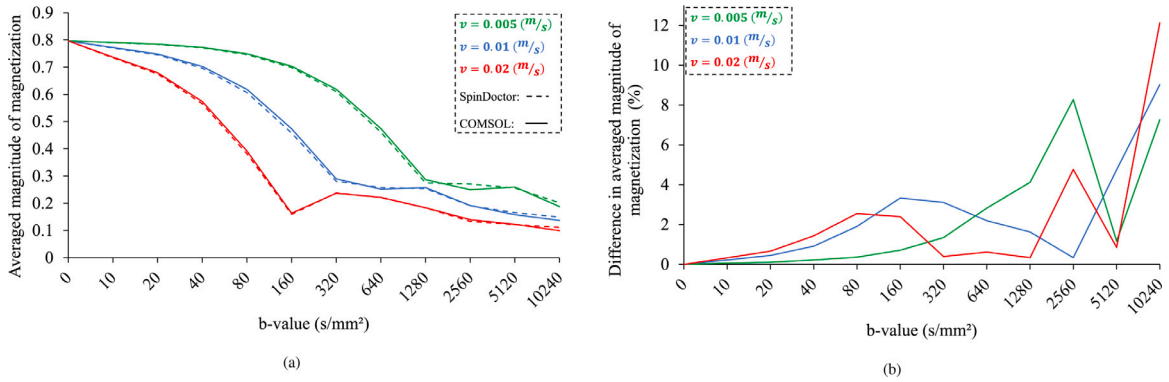

Fig. 8. Comparison between magnetisation resulting from SpinDoctor-IVIM and COMSOL for a cylinder with the radius of 5 μm and length of 100 μm: (a) Averaged magnitude of magnetisation, (b) Difference in the normalised magnitude of magnetisation.

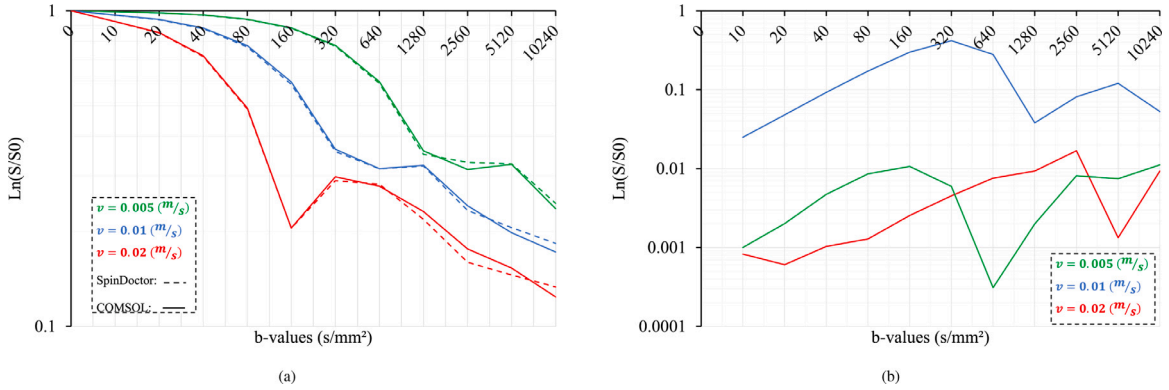

Fig. 9. Comparison between signal intensity resulting from SpinDoctor-IVIM and COMSOL for a cylinder with the radius of 5 μm and length of 100 μm: (a) Normalised signal, (b) Difference in the normalised signal. The subscripts 's' and 'c' indicate the signals of SpinDoctor-IVIM and COMSOL, respectively.

oscillatory behaviour observed above $b = 160\,\mathrm{s\,mm^{-2}}$ in Figs. 8 and 9 likely derives from destructive interference of the magnetisation of spins bounced back from the ends of the tube with the other spins. In addition, although in real-world IVIM imaging experiments, the b-value up to $300\,\mathrm{s\,mm^{-2}}$ is used, the finite element solution for the gBT equation should be valid for both IVIM (lower b-values) and regular diffusion MRI experiments (higher b-values). Hence, to validate the gBT equation solution for general dMRI simulation, we compared the results of COMSOL and SpinDoctor-IVIM up to a b-value of $10000\,\mathrm{s\,mm^{-2}}$.

6. Experiments and results

This section illustrates how the proposed tool can be used in IVIM imaging studies through some prototypical experiments.

As described earlier in Section 1, when blood flows incoherently inside a microvasculature, diffusion gradients dephase spins in the blood, which according to IVIM theory results in more signal loss in the measured signal. The IVIM theory models the capillaries' contribution to the IVIM signal based on two flow regimes of diffusive and ballistic. The diffusive regime assumes numerous changes in flow direction during the measurement. Le Bihan et al. (1986) described this signal through a bi-exponential model, which includes a true diffusion component related to the Brownian motion of water molecules, D, and a diffusion component related to perfusion that concerns blood microcirculation in the capillary network, termed pseudo-diffusion coefficient D^*, according to the following formula:

$$\frac{S}{S_0} = (1-f)\times e^{-b\times D} + f\times e^{-b\times(D^*)} \tag{22}$$

where f is the perfusion fraction. In contrast, the ballistic regime entails blood flow that maintains a consistent direction during diffusion. Here, a *sinc* function is employed to depict the signal attenuation effects, which are dependent on blood flow velocity (v) (Scott et al., 2021).

$$\frac{S}{S_0} = (1-f)\times e^{-b\times D} + f\times e^{-b\times(D_b)}\times sinc(cv) \tag{23}$$

where $c = \Delta\times(b/(\Delta-\delta/3))^{\frac{1}{2}}$.

Fig. 10(a), 10(b), and 10(c) show the distributions of vessel segments and velocity magnitudes at $v_{max} = 0.01\,\mathrm{m\,s^{-1}}$ and $v_{max} = 0.02\,\mathrm{m\,s^{-1}}$ in the ROI, respectively. The average displacement of spins during measurement time ($\Delta+\delta = 42.5\,\mathrm{ms}$) at $v_{max} = 0.01\,\mathrm{m\,s^{-1}}$ and $v_{max} = 0.02\,\mathrm{m\,s^{-1}}$, shown in Figs. 10(b) and 10(c), are 19.1 μm and 38.2 μm, respectively. When comparing these average displacements of spins with the average length of vessel segments in ROI (60.28 μm), the simulated IVIM imaging signal falls into the ballistic regime.

In the following experiments, we evaluate the effects of changes in biophysical parameters of the simulation domain, such as blood pressure (represented by blood velocity), vascular permeability (P), and intravascular diffusivities (D_b), on simulated IVIM imaging signals, as well as their effects on the estimated parameters of Eqs. (22) and (23). In this study, five models are fitted to the IVIM imaging signal including segmented model (Jalnefjord et al., 2018), Bayesian model (Gustafsson et al., 2018), adaptive model (Manjón et al., 2010), TopoPro model (Fadnavis et al., 2021), and a ballistic-based model (Scott et al., 2021).

6.1. Effect of different blood pressure on IVIM imaging signal

The connection between high blood pressure and damage to the heart, brain, retina, kidneys, and arterial blood vessels has been established in prior research (Mensah, 2016). When blood pressure exceeds

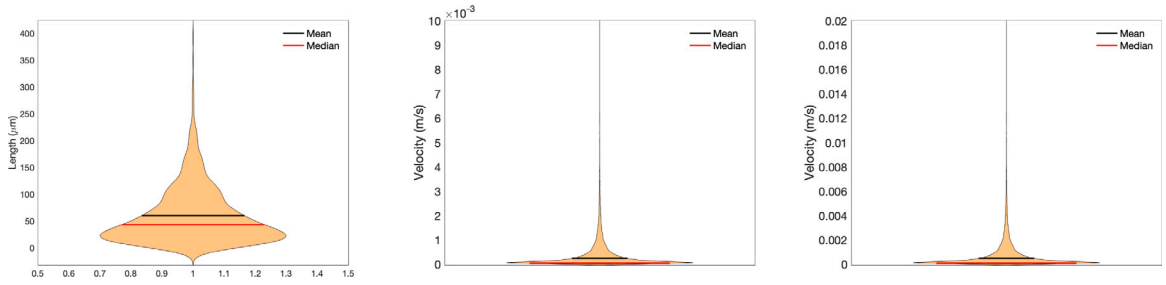

Fig. 10. (a) The distributions of vessel segments in the ROI with an average of 60.28 μm and median of 43 μm; (b) The distribution of magnitudes of velocities at $v_{max} = 0.01\,\mathrm{m\,s^{-1}}$ with an average of $450\,\mu\mathrm{m\,s^{-1}}$ and median of $96.7\,\mu\mathrm{s^{-1}}$; (c) The distribution of magnitudes of velocities at $v_{max} = 0.02\,\mathrm{m\,s^{-1}}$ with an average of $900\,\mu\mathrm{m\,s^{-1}}$ and median of $193.45\,\mu\mathrm{m\,s^{-1}}$.

the normal range, structural changes occur in the targeted organs leading to organ dysfunction (Suvila and Niiranen, 2022). This experiment aims to explore the impact of blood pressure fluctuations on IVIM imaging signals and the estimated parameters of the models in Eqs. (22) and (23).

For this purpose, in the simulation, changes in blood pressure are accommodated by modifying the velocity within the gBT equation, i.e., Eq. (15). This approach is employed because blood pressure and blood velocity are inherently interconnected. The simulated signals, resulting from this experiment, are shown in Fig. 11, where the plots in the top row show the simulated signals at a velocity of $0.01\,\mathrm{ms^{-1}}$, while the bottom row shows the simulated signals at a velocity of $0.02\,\mathrm{ms^{-1}}$.

6.2. Effect of different intravascular diffusivities on IVIM imaging signal

According to typical IVIM imaging experiments, the effect of blood self-diffusion on signal attenuation is trivial compared to blood velocity (modelled by pseudo-diffusion), but the results of the flow-compensated diffusion gradient experiment do not support this assertion (Funck et al., 2018). The objective of this experiment is to investigate whether alterations in D_b affect the simulated IVIM imaging signals and the estimation of parameters in Eqs. (22) and (23). To achieve this, we employ two distinct D_b values of $10^{-10}\mathrm{mm^2/s}$ and $126 \times 10^{-5}\mathrm{mm^2/s}$ —The value of $126\times10^{-5}\mathrm{mm^2/s}$ is the experimental coefficient of blood diffusivity reported in Funck et al. (2018). Fig. 11 shows the simulated signals in which the variations in colours denote different values of D_b.

6.3. Effect of different vascular permeabilities on IVIM imaging signal

The permeability of the vascular system refers to the rate at which molecules and solutes exchange between the inside and outside of the vessel. Maintaining tissue function in a healthy physiological state requires normal/regular exchange between blood components and tissues. Several vasculopathies have the ability to modulate and alter this exchange rate, adversely affecting tissue function (Wautier and Wautier, 2022). Here are some examples: An increase in tumour microvascular permeability helps with cancer metastatic spread; Acute increases in myocardial permeability result in tissue oedema, affecting the pumping efficiency of the heart, as highlighted by Claesson-Welsh (2015); An increase in permeability increases interstitial pressure and affects the delivery of therapeutic agents; An increase in retina microvasculature permeability is one of the first observable alterations in diabetic retinopathy, which can cause vision loss (Antonetti et al., 1999). As discussed in Section 1.2, previous simulation tools do not account for the effect of P on simulated signals. The objective of this experiment is to investigate the impact of alterations in P on the IVIM imaging signal and to assess whether the IVIM signal models in Eqs. (22) and (23) can effectively detect these variations. This is accomplished by simulating the IVIM imaging signal within the retinal microvasculature using different orders of magnitude for P values: $10^{-7}\,\mathrm{m\,s^{-1}}$, $10^{-6}\,\mathrm{m\,s^{-1}}$ (Allen et al., 2020), $10^{-5}\,\mathrm{m\,s^{-1}}$ (Allen et al., 2021), and $10^{-4}\,\mathrm{m\,s^{-1}}$. In Fig. 11, different markers are used to represent the resulting signals corresponding to the different values of P.

All described experiments maintain fixed values for the following imaging and biophysical parameters:

- A classic Stejskal–Tanner pulse sequence is used for the IVIM imaging simulation, with b-values ranging from $0\,\mathrm{s/\mu m^2}$ to $800\,\mathrm{s/\mu m^2}$ with the incremental step of $50\,\mathrm{s/\mu m^2}$.
- Fixed diffusion time and gradient duration of 40 ms and 2.5 ms are used, while gradient ramps are neglected.
- Intravascular and extravascular T_2 relaxations are fixed 30.5 ms (Lin et al., 2012) (the average value of T_2 for arterial and venous blood) and 25 ms (Chen et al., 2008), respectively.
- The fixed value of $50 \times 10^{-5}\,\mathrm{mm^2/s}$ is used for the diffusivity in the extravascular space (Chen et al., 2008).

Figs. 11(a) and 11(c) show the IVIM imaging signal decay at the different b-values, originating from both intravascular and extravascular spaces, for the different values of D_b (indicated by different colours) and P (indicated by different markers). At the same time, the maximum blood velocity within the microvasculature is $0.01\,\mathrm{m\,s^{-1}}$ and $0.02\,\mathrm{m\,s^{-1}}$ for the top and bottom, respectively. Similarly, Figs. 11(b) and 11(d) display the same information about the decay of the IVIM imaging signal originating only from the intravascular space (the intravascular signal is isolated by integrating the product of the mass matrix of Eq. (17) and the magnetisation of the tetrahedrons located in the intravascular space). A significant error is clearly observed in diagrams of Fig. 11 when D_b is excluded from the simulation of IVIM imaging signal. In addition, an increase in P increases signal decay in Fig. 11. Furthermore, comparing Fig. 11(a) with 11(c) and Fig. 11(b) with 11(d), respectively, shows an increase in the signal decay rate in IVIM imaging as the v increases.

Figs. 12, 13, 14, and 15 compare changes in the estimated values of D^*, D, f, and v for different values of P, D_b, and v. Fig. 12 shows that including D_b reduces the estimated value of D^* across all models. However, the estimated value of D^* increases as v increases, and decreases with higher values of P regardless of D_b. As shown in Fig. 13, considering D_b increases the estimated value of D for all models. Additionally, when D_b is included, the estimated value of D decreases with an increase in v, as expected, which is not the case when D_b is excluded. However, the higher P increases the estimated value of D regardless of D_b, only observed in the results of the segmented, adaptive, and ballistic models. With perfusion fraction, a higher v, D_b, and P result in higher estimated values of f, shown in Fig. 14. The volume fraction of the microvasculature in the experimental ROI, shown in Fig. 5, is around 7.62%, and only the ballistic model has the closest estimation. Finally, as shown in Fig. 15, the estimated velocity (v_e) using the ballistic model decreases when D_b is included. However, v_e increases with an increase in v and decreases with an increase in P,

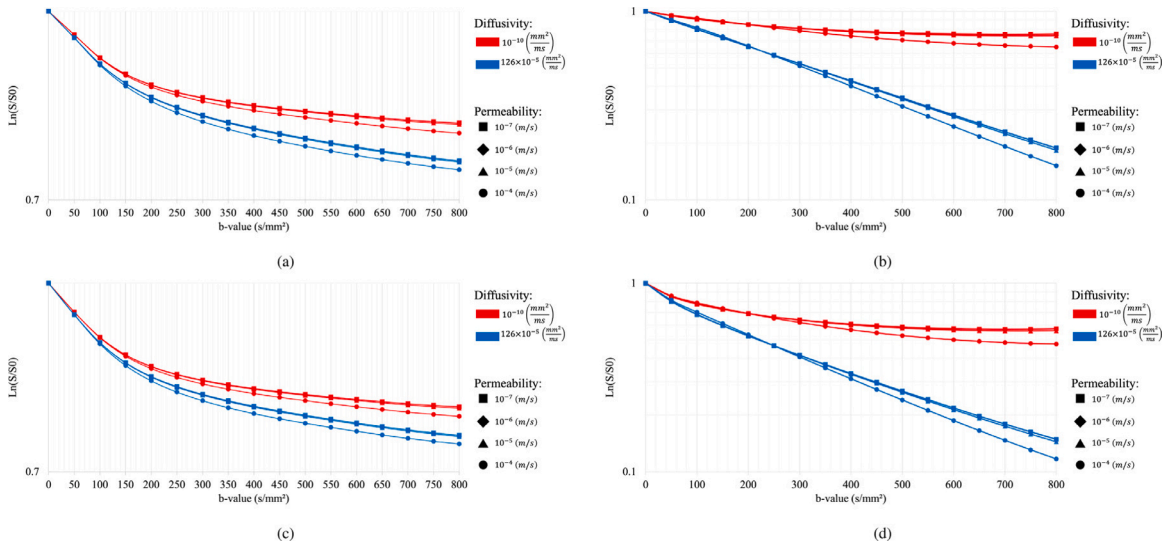

Fig. 11. Effect of changing D_b and P on (a) IVIM imaging signal originated from both intravascular and extravascular spaces at the velocity of $0.01\,\mathrm{m\,s^{-1}}$, (b) IVIM imaging signal originated from intravascular spaces at the velocity of $0.01\,\mathrm{m\,s^{-1}}$, (c) IVIM imaging signal originated from both intravascular and extravascular spaces at the velocity of $0.02\,\mathrm{m\,s^{-1}}$, and (d) IVIM imaging signal originated from intravascular spaces at the velocity of $0.02\,\mathrm{m\,s^{-1}}$.

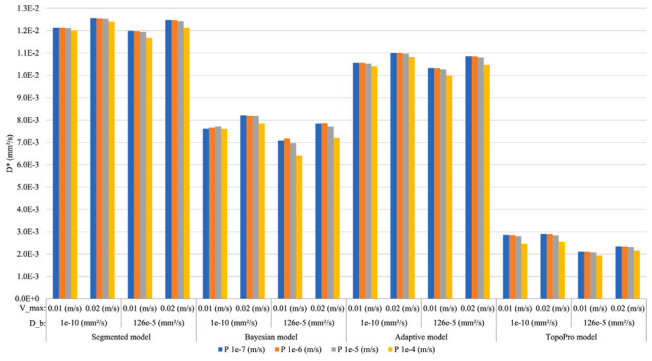

Fig. 12. The estimated value of D^* at the different v, D_b and P using the different models.

regardless of D_b. Moreover, compared to the median/mean velocities of the simulated distribution shown in Fig. 10, the ballistic model estimates v_e at the same order of magnitude ($0-1\,\mathrm{mm\,s^{-1}}$).

Caution must be applied to interpret the above findings as they might not be generalisable to more complex geometries, as the microvasculature used here has a simple geometry and is small. Furthermore, here we consider the same values of T_2 for all segments of the vessel, while the values of T_2 of blood depend on the hematocrit content and the oxygenation level (Lin et al., 2012), which can affect the results of this study.

6.4. Computational cost

The simulations in Section 5 were performed on ARC3, the High-Performance Computing facilities at the University of Leeds. ARC3 consists of 252 nodes with 24 cores (Broadwell E5-2650v4 CPUs, 2.2 GHz) and 128 GB of memory each, and an SSD within the node with 100 GB of storage. The details of the computational cost for the simulations undertaken in Section 5 are reported in Table 1.

7. Discussion

This study introduces SpinDoctor-IVIM, a virtual imaging tool designed to simulate IVIM imaging signals using a new finite element solver for gBT PDE. SpinDoctor-IVIM offers a more realistic and comprehensive means of simulating IVIM imaging, serving as a valuable resource for prototyping in this field. One of the more significant findings emerging from this study is the substantial impact of D_b on the IVIM imaging signal, which is in agreement with previous research (Funck et al., 2018). As shown in Figs. 12, 13, 14, and 15, including D_b in the simulation greatly impacts the estimated values of D^*, D, f, and v_e. Furthermore, as shown in Fig. 13, the exclusion of D_b reverses the trends of changes in estimated D due to changes in v, emphasising the importance of including D_b in simulations. Additionally, the important role of D_b can be supported theoretically since the gBT equation is similar to the convection–diffusion equation, as it includes both convection, i.e., $\boldsymbol{v}(\boldsymbol{r},t)\cdot\nabla M_I(\boldsymbol{r},t)$, and diffusion, i.e., $\nabla\cdot(D_I(\boldsymbol{r})\nabla M_I(\boldsymbol{r},t))$, terms in intravascular space. There is evidence that the solutions of the convection–diffusion equation are dependent on the diffusion coefficient, and the diffusion coefficient strongly influences the numerical behaviour of the solution (Verdickt et al., 2006).

Furthermore, this study illustrates the influence of P on the simulated IVIM imaging signal. These effects cannot be explored using the previous numerical method (Fournet et al., 2017; Mozumder et al., 2018; Suvila and Niiranen, 2022; Van et al., 2021), as these methods simulate IVIM imaging signals solely by modelling spin movements along vascular trajectories, which limits consideration of intravascular diffusivity, and permeability exchange between intravascular and extravascular spaces.

As well as these advantages of the proposed tool, the simulated signal is calculated based on a more realistic blood flow simulation. This enhancement in methodology improves the reliability of the results and enables localised exploration of the connection between blood flow parameters, such as blood velocity, and vessel wall shear stress with IVIM imaging parameters. Hence, the tool proposed here lays the groundwork for future research on the numerical study of IVIM imaging.

One source of weakness in this study, which can affect the measurements in Fig. 12, 13, 14, and 15 was the limitation of access to a complex and large microvasculature and real IVIM imaging data for a comprehensive analysis of the sensitivity of the IVIM imaging signal to changes in imaging parameters and biophysical parameters of the microvasculature. In addition, due to the small size of the microvasculature, the range of possible values for the velocity of blood flow and the diffusion encoding time was limited during the simulations to preserve

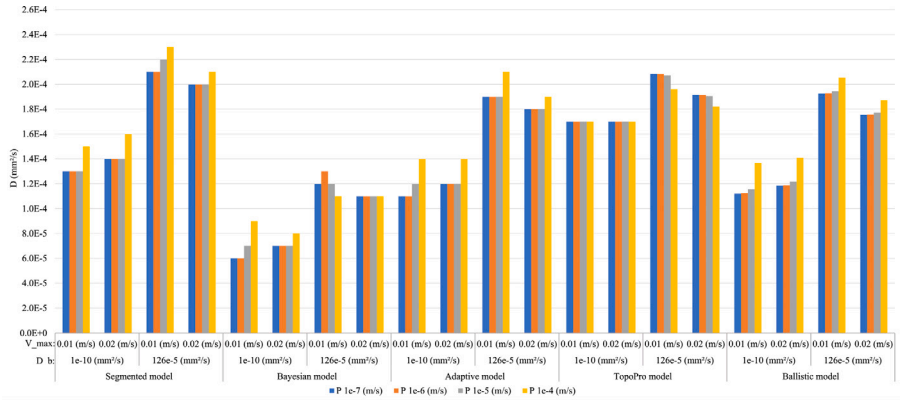

Fig. 13. The estimated value of D at the different v, D_b and P using the different models.

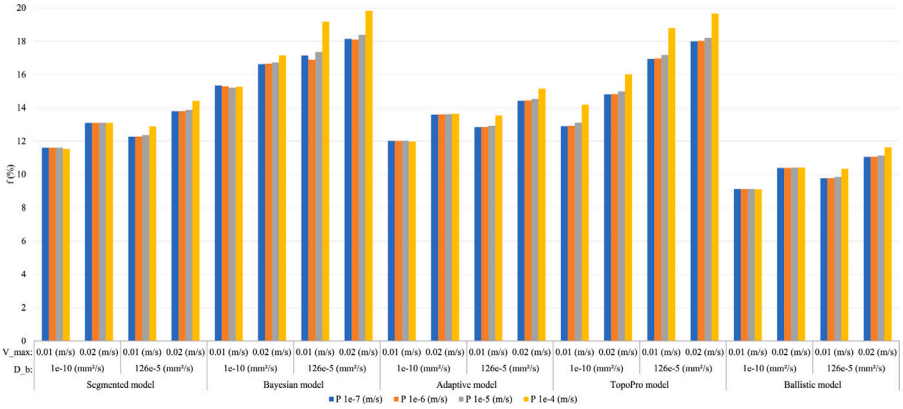

Fig. 14. The estimated value of f at the different v, D_b and P using the different models.

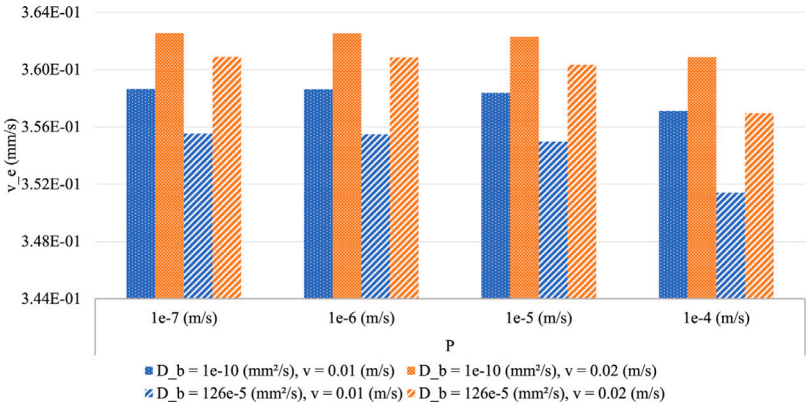

Fig. 15. The estimated value of v_e at the different v, D_b and P using the different models.

Table 1
Computational cost of the simulation.

The number of nodes in the mesh	Memory per core (GB)	Number of cores per signal simulation over 17 b-values	Average of computational time (core hours)
224 327	6	12	11

larger portion of the microvasculature by minimising $\max\{\boldsymbol{v}(\boldsymbol{r},t)\}\times T_e$, introduced in Section 4.4. Furthermore, the T_2 values of the blood depend on the haematocrit content and the level of oxygenation. Hence, different types of vessels, that is, arterial and venous, have a specific range of T_2 values (Lin et al., 2012). Having more information about the type of vessels would allow for a more accurate IVIM imaging simulation by assigning realistic values to T_2 relaxation. Therefore, additional work is needed to label the different types of vessels in the microvasculature mesh so that the simulation parameters are set with an appropriate distribution of T_2 relaxation.

8. Conclusion

In conclusion, this paper introduces a significant advancement in the field of IVIM imaging through the development of a virtual imaging tool, SpinDoctor-IVIM. By leveraging an innovative finite element solver and integrating with HemeLB for blood flow simulations, this tool allows for the efficient design, evaluation, and optimisation of novel approaches in IVIM imaging. Unlike previous methods, SpinDoctor-IVIM uniquely considers the volumetric microvasculature during blood flow simulations, incorporates diffusion phenomena in the intravascular space, and represents the permeability between intravascular and extravascular spaces. The proposed virtual IVIM imaging approach offers a promising avenue to expedite the validation process of IVIM-related quantitative models by bridging the gap between observable markers in imaging and underlying pathophysiological mechanisms. Additionally, it can provide recommendations for IVIM acquisition parameters to the IVIM imaging community. Therefore, SpinDoctor-IVIM presents a valuable tool to propel advancements in clinical MRI and enhance our understanding of tissue perfusion and diffusion dynamics.

CRediT authorship contribution statement

Mojtaba Lashgari: Writing – review & editing, Writing – original draft, Visualization, Validation, Software, Investigation, Conceptualization. **Zheyi Yang:** Writing – review & editing, Software. **Miguel O. Bernabeu:** Software, Data curation. **Jing-Rebecca Li:** Writing – review & editing, Supervision, Software. **Alejandro F. Frangi:** Writing – review & editing, Supervision, Resources, Project administration, Investigation, Funding acquisition, Conceptualization.

Declaration of competing interest

The authors declare that they have no known competing financial interests or personal relationships that could have appeared to influence the work reported in this paper.

Acknowledgements

ML was an Early Career Researcher funded by the European Union's Horizon 2020 Research and Innovation Programme under the Marie Skodowska-Curie Innovative Training Network B-Q MINDED (H2020-MSCA-ITN-2017-764513). AFF acknowledges support from the Royal Academy of Engineering under the RAEng Chair in Emerging Technologies, United Kingdom (INSILEX CiET1919/19) and the ERC Advanced Grant – UKRI Frontier Research Guarantee (INSILICO EP/Y030494/1) schemes. MOB gratefully acknowledges funding from: Foundation Leducq Transatlantic Network of Excellence (17 CVD 03); EPSRC, United Kingdom grant no. EP/X025705/1; British Heart Foundation and The Alan Turing Institute Cardiovascular Data Science Award (C-10180357); the SCONe projects funded by Chief Scientist Office, Edinburgh and Lothians Health Foundation, Sight Scotland, the Royal College of Surgeons of Edinburgh, United Kingdom, the RS Macdonald Charitable Trust, and Fight For Sight. Furthermore, computations in this work were performed on ARC3 and ARC4, the High-Performance Computing facilities at the University of Leeds, UK, and Amazon Web Services through our MULTI-X middleware platform (www.multix.org). Finally, the authors acknowledge helpful discussions with Dr. M Mozumder, Dr. *N* Ravikumar, and Dr. R Enjalbert in the different phases of this work.

Data availability

The data that has been used is confidential.

References

Allen, C.L., Malhi, N.K., Whatmore, J.L., Bates, D.O., Arkill, K.P., 2020. Non-invasive measurement of retinal permeability in a diabetic rat model. Microcirculation 27 (6), e12623.

Allen, C.L., Wolanska, K., Malhi, N.K., Benest, A.V., Wood, M.E., Amoaku, W., Torregrossa, R., Whiteman, M., Bates, D.O., Whatmore, J.L., 2021. Hydrogen sulfide is a novel protector of the retinal glycocalyx and endothelial permeability barrier. Front. Cell Dev. Biol. 9, 724905.

Amidror, I., 2002. Scattered data interpolation methods for electronic imaging systems: A survey. J. Electron. Imaging 11 (2), 157–176.

Antonetti, D.A., Lieth, E., Barber, A.J., Gardner, T.W., 1999. Molecular mechanisms of vascular permeability in diabetic retinopathy. In: Seminars in Ophthalmology, vol. 14, (4), Taylor & Francis, pp. 240–248.

Baieth, H.A., 2008. Physical parameters of blood as a non-Newtonian fluid. Int. J. Biomed. Sci.: IJBS 4 (4), 323.

Bernabeu, M.O., Jones, M.L., Nielsen, J.H., Krüger, T., Nash, R.W., Groen, D., Schmieschek, S., Hetherington, J., Gerhardt, H., Franco, C.A., et al., 2014. Computer simulations reveal complex distribution of haemodynamic forces in a mouse retina model of angiogenesis. J. R. Soc. Interface 11 (99), 20140543.

Besl, P.J., McKay, N.D., 1992. Method for registration of 3-D shapes. In: Sensor Fusion IV: Control Paradigms and Data Structures, vol. 1611, Spie, pp. 586–606.

Chen, Y., Medioni, G., 1992. Object modelling by registration of multiple range images. Image Vis. Comput. 10 (3), 145–155.

Chen, J., Wang, Q., Zhang, H., Yang, X., Wang, J., Berkowitz, B.A., Wickline, S.A., Song, S.K., 2008. In vivo quantification of T1, T2, and apparent diffusion coefficient in the mouse retina at 11.74 T. Magn. Reson. Med.: Official J. Int. Soc. Magn. Reson. Med. 59 (4), 731–738.

Claesson-Welsh, L., 2015. Vascular permeability—the essentials. Upsala J. Med. Sci. 120 (3), 135–143.

Fadnavis, S., Endres, S., Wen, Q., Wu, Y.C., Cheng, H., Koudoro, S., Rane, S., Rokem, A., Garyfallidis, E., 2021. Bifurcated topological optimization for IVIM. Front. Neurosci. 15, 779025.

Federau, C., 2017. Intravoxel incoherent motion MRI as a means to measure in vivo perfusion: A review of the evidence. NMR Biomed. 30 (11), e3780.

Federau, C., O'Brien, K., Meuli, R., Hagmann, P., Maeder, P., 2014. Measuring brain perfusion with intravoxel incoherent motion (IVIM): initial clinical experience. J. Magn. Reson. Imaging 39 (3), 624–632.

Fieremans, E., Lee, H.H., 2018. Physical and numerical phantoms for the validation of brain microstructural MRI: A cookbook. Neuroimage 182, 39–61.

Fournet, G., Li, J.R., Cerjanic, A.M., Sutton, B.P., Ciobanu, L., Le Bihan, D., 2017. A two-pool model to describe the IVIM cerebral perfusion. J. Cereb. Blood Flow Metab. 37 (8), 2987–3000.

Franco, C.A., Mericskay, M., Parlakian, A., Gary-Bobo, G., Gao-Li, J., Paulin, D., Gustafsson, E., Li, Z., 2008. Serum response factor is required for sprouting angiogenesis and vascular integrity. Dev. Cell 15 (3), 448–461.

Funck, C., Laun, F.B., Wetscherek, A., 2018. Characterization of the diffusion coefficient of blood. Magn. Reson. Med. 79 (5), 2752–2758.

Gustafsson, O., Montelius, M., Starck, G., Ljungberg, M., 2018. Impact of prior distributions and central tendency measures on Bayesian intravoxel incoherent motion model fitting. Magn. Reson. Med. 79 (3), 1674–1683.

Iima, M., Le Bihan, D., 2016. Clinical intravoxel incoherent motion and diffusion MR imaging: past, present, and future. Radiology 278 (1), 13–32.

Jalnefjord, O., Andersson, M., Montelius, M., Starck, G., Elf, A.K., Johanson, V., Svensson, J., Ljungberg, M., 2018. Comparison of methods for estimation of the intravoxel incoherent motion (IVIM) diffusion coefficient (D) and perfusion fraction (f). Magn. Reson. Mater. Phys. Biol. Med. 31, 715–723.

Jerome, N.P., Caroli, A., Ljimani, A., 2021. Renal diffusion-weighted imaging (DWI) for apparent diffusion coefficient (ADC), intravoxel incoherent motion (IVIM), and diffusion tensor imaging (DTI): basic concepts. In: Preclinical MRI of the Kidney: Methods and Protocols. Springer US, pp. 187–204.

Le Bihan, D., Breton, E., Lallemand, D., Grenier, P., Cabanis, E., Laval-Jeantet, M., 1986. MR imaging of intravoxel incoherent motions: application to diffusion and perfusion in neurologic disorders. Radiology 161 (2), 401–407.

Li, J.R., Nguyen, V.D., Tran, T.N., Valdman, J., Trang, C.B., Van Nguyen, K., Vu, D.T.S., Tran, H.A., Tran, H.T.A., Nguyen, T.M.P., 2019. SpinDoctor: A matlab toolbox for diffusion MRI simulation. NeuroImage 202, 116120.

Lin, A.L., Qin, Q., Zhao, X., Duong, T.Q., 2012. Blood longitudinal (T 1) and transverse (T 2) relaxation time constants at 11.7 Tesla. Magn. Reson. Mater. Phys. Biol. Med. 25, 245–249.

Manjón, J.V., Coupé, P., Martí-Bonmatí, L., Collins, D.L., Robles, M., 2010. Adaptive non-local means denoising of MR images with spatially varying noise levels. J. Magn. Reson. Imaging 31 (1), 192–203.

Mazzeo, M.D., Coveney, P.V., 2008. HemeLB: A high performance parallel lattice-Boltzmann code for large scale fluid flow in complex geometries. Comput. Phys. Comm. 178 (12), 894–914.

Mensah, G.A., 2016. Hypertension and target organ damage: don't believe everything you think!. Ethnicity Dis. 26 (3), 275.

Mozumder, M., Beltrachini, L., Collier, Q., Pozo, J.M., Frangi, A.F., 2018. Simultaneous magnetic resonance diffusion and pseudo-diffusion tensor imaging. Magn. Reson. Med. 79 (4), 2367–2378.

Oliveira, I.S., 2021. NMR of confined fluids: A numerical study using COMSOL with application in petrophysics. arXiv preprint arXiv:2105.11395.

Scott, L.A., Dickie, B.R., Rawson, S.D., Coutts, G., Burnett, T.L., Allan, S.M., Parker, G.J., Parkes, L.M., 2021. Characterisation of microvessel blood velocity and segment length in the brain using multi-diffusion-time diffusion-weighted MRI. J. Cereb. Blood Flow Metab. 41 (8), 1939–1953.

Spinner, G.R., Stoeck, C.T., Mathez, L., von Deuster, C., Federau, C., Kozerke, S., 2019. On probing intravoxel incoherent motion in the heart-spin-echo versus stimulated-echo DWI. Magn. Reson. Med. 82 (3), 1150–1163.

Stuart, A.M., Peplow, A., 1991. The dynamics of the theta method. SIAM J. Sci. Stat. Comput. 12 (6), 1351–1372.

Suvila, K., Niiranen, T.J., 2022. Interrelations between high blood pressure, organ damage, and cardiovascular disease: no more room for doubt. Hypertension 79 (3), 516–517.

Tennyson, C., 2014. Lattice Boltzmann method for integrating the Bloch equation in muscle fibers and microvessels.

Van, V.P., Schmid, F., Spinner, G., Kozerke, S., Federau, C., 2021. Simulation of intravoxel incoherent perfusion signal using a realistic capillary network of a mouse brain. NMR Biomed. 34 (7), e4528.

Verdickt, L., Voitovich, T., Vandewalle, S., Lust, K., Smets, I., Van Impe, J., 2006. Role of the diffusion coefficient in one-dimensional convection–diffusion models for sedimentation/thickening in secondary settling tanks. Math. Comput. Model. Dyn. Syst. 12 (5), 455–468.

Wautier, J.L., Wautier, M.P., 2022. Vascular permeability in diseases. Int. J. Mol. Sci. 23 (7), 3645.

Zhang, X., Ingo, C., Teeuwisse, W.M., Chen, Z., van Osch, M.J., 2018. Comparison of perfusion signal acquired by arterial spin labeling–prepared intravoxel incoherent motion (IVIM) MRI and conventional IVIM MRI to unravel the origin of the IVIM signal. Magn. Reson. Med. 79 (2), 723–729.